PROCEEDINGS A

rspa.royalsocietypublishing.org

Research

Article submitted to journal

**Subject Areas:**
Applied Mathematics, Wave Physics, Scattering Theory

**Keywords:**
Tuneable Metamaterial, Metacylinder, Metagrating, Rayleigh-Bloch Modes, Diffraction Grating

**Author for correspondence:**
H.J. Putley
e-mail: h.putley18@imperial.ac.uk

# A Tuneable Electromagnetic Metagrating

H. J. Putley[1], S. Guenneau[1,2], R. Porter[3] and R.V. Craster[1,2]

[1]Department of Mathematics, Imperial College London, London, SW7 2AZ, UK
[2]UMI 2004 Abraham de Moivre-CNRS, Imperial College London, London, SW7 2AZ, UK
[3]School of Mathematics, University of Bristol, Bristol, BS8 1UG, UK

We explore electromagnetic (EM) wave incidence upon gratings of reconfigurable metamaterial cylinders, that collectively act as a metagrating, to identify their potential as reconfigurable subwavelength surfaces. The metacylinders are created by a closely-spaced microstructured internal array of thin plates that, in the limit of small inter-plate spacing, are described by a semi-analytical continuum model. We build upon metacylinder analysis in water waves, translating this to EM for TE polarization (longitudinal magnetic field) for which the metacylinders exhibit anisotropic scattering and internal trapping; these features are exploited for the multiple scattering of light by an infinite metagrating of uniform cylinder radius and angle, for which we retrieve the far-field reflection and transmission spectra for plane-wave incidence. These spectra reveal unusual effects including perfect reflection and a negative Goos-Hänchen shift in the transmitted field, as well as perfect symmetry in the far-field scattering coefficients even under non-normal incident angle. The metagrating also hosts exclusively symmetric Rayleigh-Bloch surface-waves whose dispersion is contingent on the uniform cylinder angle, shifting under rotation towards the light-line as the cylinder angle approaches the horizontal. For both plane-wave scattering and the calculation of the array-guided modes, the cylinder angle is the principal variable in determining the wave interaction, and the metagrating is tuneable simply through rotation of the constituent metacylinders.



THE ROYAL SOCIETY PUBLISHING

## 1. Introduction

The interaction of EM waves with circular cylinders, of infinite extent in the axial direction, is well-studied across wave physics, for instance for obliquely incident waves in photonic crystals formed from singly- and doubly-periodic arrays of cylinders [1]. The invariance of the solution in depth, along with the radial symmetry of the cylinders, leads to the surrounding wavefield being fully described by multipole expansions in Fourier coefficients and Bessel and Hankel functions [2]. The elegance of multipole expansions in terms of encapsulating the interaction of waves with any number and arrangement of circular objects has made it an invaluable tool in the arsenal of wave physicists, and it has been used to describe all manner of complex wave phenomena: examples include multiple scattering [3], the existence of trapped and guided modes [4,5], the diffraction theory of gratings [6,7] and exploring band-gaps and filtering in photonic and phononic crystals [1,8,9] amongst many others. We aim to extend this style of analysis to metagratings constructed by internally structured metacylinders and utilize this elegant formalism to study metagratings as shown in Fig. 1.

Of particular relevance to this aim are the articles by Evans, Porter, Linton and the McIvers *et al.* on the guiding and scattering of waves by singly-periodic arrays, i.e. gratings, of impermeable cylinders [4,10–13], which we can draw upon and exploit. An important feature of some periodic gratings is the presence of the array-guided modes; the existence of array-guided or Rayleigh-Bloch surface-waves along gratings of impermeable cylinders of Neumann boundary condition was proven in [11,12] and for general structures in [14], whereas those of Dirichlet boundary condition do not host Rayleigh-Bloch modes [15]. Rayleigh-Bloch modes are classified as waves that propagate solely along the grating and experience exponential decay with perpendicular distance from the grating axis. Their existence has implications for the kinds of solutions that will be observed in the scattering of light by infinite and truncated gratings, and hence the forces experienced by cylinders along the grating.

Recently, Porter *et al.* have published a series of works on plate array metamaterials, for water waves, that exhibit novel wave interactions [16–20]. In [17] Porter considers a closely-spaced periodic array of thin plates of Neumann boundary condition and identical height and tilt angle, and uses the close spacing of the plates to approximate the plate array as an effective medium described simply by a one-dimensional wave equation. This continuum model stipulates that the plate array acts as a perfectly-transmitting negative-refraction metamaterial, capable of perfect waveshifting across the medium as well as being entirely transparent to a plane-wave when the angle of incidence and tilt angle equate. This has been further developed upon by Porter and Zheng to consider cylinders of circular cross-section composed of the same plate array medium [18–20], being referred to as metamaterial cylinders or metacylinders. In particular in [18] the metacylinders have been used to redirect wave energy for the purposes of focusing and blocking water waves, and the capabilities of energy dissipation within the effective medium have been explored. The scattering of incident radiation by the metacylinder has been found to point primarily along the direction at a right angle to the plate array angle, with little-to-no scattered energy propagation through the exterior domain along the direction of the plate array. As such, this motivates us to explore the reflection and transmission spectra belonging to a periodic one-dimensional grating of evenly spaced metacylinders, or metagrating, to determine if such a metagrating will be highly dependent on the choice of uniform cylinder angle belonging to all constituent metacylinders, and reflect the fact that the metagrating should be entirely transparent to an incident wave of any wavenumber that points in the same direction as the plate array. Given the existence of Rayleigh-Bloch modes for both gratings of impermeable plates [14] and impermeable circular cylinders [4], and their importance for scattering and energy transport, one expects the metagrating could host Rayleigh-Bloch modes and moreover that they could be tuneable through rotation of the uniform cylinder angle.

The purpose of this work is to recast Porter's metacylinders in electromagnetism, and to model their interaction with TE polarized light under oblique incidence. In § 2 we provide a brief

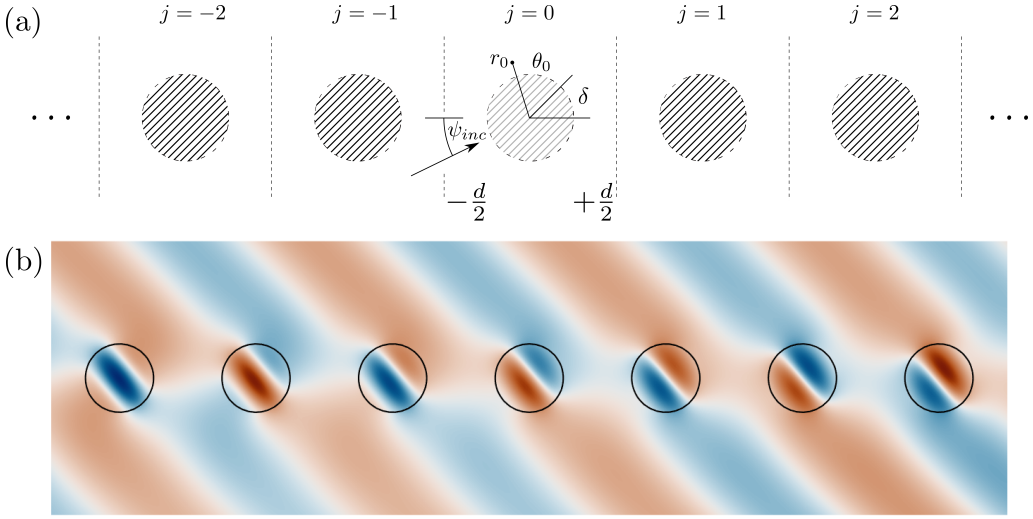


**Figure 1.** (a) Cross-section of the infinite metagrating. (b) A negative Goos-Hänchen shift in the transmitted field due to the scattering of a plane-wave of incident angle $\psi_{\text{inc}} = \pi/4$ by a metagrating of uniform angle $\delta = -0.926$.

description of the oblique incidence of light on a set of metamaterial cylinders of circular cross-section invariant along their infinite length, including a description of the multipole expansions defining the wavefield in the exterior domain and the continuum model encapsulating the plate array metamaterial. The scattering of a plane-wave by an arbitrarily arranged set of metacylinders is set out in § 2(d), for which we observe the aforementioned anisotropic scattering and trapping behaviours characteristic of the metamaterial. In developing this scattering theory we solve for the scattering by an infinite metagrating in § 3, see Fig. 1, by making use of Twersky's rapidly convergent elementary function representation for the infinite sum over the cylinders [21]. We extract the reflection and transmission coefficients following Linton's method [13], and verify the implementation of the model computationally by use of the power-balance criterion of Achenbach [22]. In a similar fashion, we search for Rayleigh-Bloch modes belonging to the infinite metagrating in § 4, finding that the metagrating hosts exclusively symmetric Rayleigh-Bloch modes that are tuneable by rotation of the uniform cylinder angle. We provide our concluding remarks in § 5 followed by Appendices A-C detailing the metacylinder continuity conditions, the scattering matrix and Twersky's elementary function representation respectively.

## 2. Problem Description

In this problem we consider the oblique incidence of an electromagnetic wave on a set of $N$ metacylinders of circular cross-section extending infinitely along the $z$-axis for which we consider a cylindrical coordinate system $(r, \theta, z)$. For light of TE polarization we define the magnetic and electric fields as $\mathbf{H} = (0, 0, H_z)$ and $\mathbf{E} = (E_r, E_\theta, 0)$ and distinguish between the domains interior to and exterior to the cylinders with the notation $\mathbf{V}^{int}$ and $\mathbf{V}^{ext}$ where $\mathbf{V}$ represents either the electric or magnetic field. Due to the invariance along $z$ of the metacylinders and the surrounding medium, both the interior and exterior fields must be periodic along the $z$ direction with

$$\mathbf{V}(r, \theta, z) = \mathbf{V}(r, \theta) e^{i\gamma z}, \tag{2.1}$$

where $\gamma \geq 0$ is the propagation constant along the $z$-axis. By assuming an implicit harmonic time dependence $\exp(-i\omega t)$, the electric and magnetic fields are solutions to the time-harmonic

Maxwell equations,

$$\begin{aligned} \nabla \cdot \mathbf{E} = 0, \quad \nabla \times \mathbf{E} = ik\sqrt{\frac{\mu}{\varepsilon}}\mathbf{H}, \\ \nabla \cdot \mathbf{H} = 0, \quad \nabla \times \mathbf{H} = -ik\sqrt{\frac{\varepsilon}{\mu}}\mathbf{E}, \end{aligned} \tag{2.2}$$

where $\mu$ is the magnetic permeability and $\varepsilon$ is the electric permittivity of the medium, and $\omega = k/\sqrt{\mu\varepsilon}$ is the angular wave frequency. Through elimination of the electric field, equations (2.2) in conjunction with (2.1) can be combined to form a Helmholtz equation for the magnetic field,

$$(\nabla^2 + k_\perp^2)H_z(r,\theta) = 0, \tag{2.3}$$

and similarly for the electric field components. Here $k_\perp = \sqrt{k^2 - \gamma^2} = k\sin(\alpha)$ and $\nabla^2$ is the Laplacian in two dimensional polar coordinates; see [6] for the derivation in full. In order to proceed, it is necessary now to discuss the metacylinder composition and the corresponding boundary conditions in order to arrive to a fully specified problem. Herein the metacylinders are themselves composed of a set of closely-spaced thin plates that allow for only forward and backward travelling waves in the interior, and continuity of the field and flux at the cylindrical boundary. See § 2(b) for the details of the effective medium in full, which relies on an assumed Neumann condition on the plate surfaces. In order to enforce this Neumann condition on the magnetic field, we insist that the plates composing the metacylinders are perfect conductors. Hence

$$\frac{\partial H_z}{\partial n} = 0, \tag{2.4}$$

for the normal $\mathbf{n}$ to the plate surfaces. Condition (2.4) also ensures that the electric and magnetic field calculations need not be carried out simultaneously; the magnetic field is determined through calculation of the requisite scattering coefficients, with the electric field following via the curl of $\mathbf{H}$ as in (2.2). See [1,23] for the derivation of (2.4) for metallic cylinders of circular cross-section. For ease of computation the material filling the interstitial cylinder space is set to match that of the exterior, for which we choose air with $\mu = \mu_0$ and $\varepsilon = \varepsilon_0$; additionally, the interstitial material can include damping.

With the problem fully specified, we separate our interior and exterior domains and solve for the multiple scattering of a TE polarized wave by a set of $N$ metacylinders. It is convenient to introduce the scaled magnetic field $\mathbf{K} = \sqrt{\mu_0/\varepsilon_0}\mathbf{H}$ so as to distinguish between the magnetic field and the Hankel functions in use throughout. Note that the following derivation of the scattering model follows closely that of Porter [17] and Zheng [18].

## (a) The Exterior Field

The expression for a wavefield exterior to a set of circular inclusions is well known, and takes advantage of the circular periodicity to express the total field in the vicinity of the cylinders as a multipole expansion in Bessel functions of the first and third kinds; see for example [1,3,5]. If a plane-wave of wavenumber $k_\perp$ and angle $\psi_{inc}$ with respect to the $x$-axis is incident on a set of $N$ cylinders, we may write the total field at any point in the exterior domain as the sum over the incident and scattered fields,

$$K_z^{ext} = \sum_{m=-\infty}^{\infty} i^m J_m(k_\perp r)e^{im(\theta-\psi_{inc})} + \sum_{l=1}^{N}\sum_{m=-\infty}^{\infty} b_{l,m}H_m(k_\perp r_l)e^{im\theta_l} \tag{2.5}$$

where the first sum represents the incident plane-wave in global coordinates $(r,\theta)$ and the second sum over $l \in [1,N]$ is known as the Wijngaard expansion and represents the scattered field contribution from all cylinders in their respective local coordinates $(r_l,\theta_l)$ [24], see Fig. 2(a). Here $J_m(x)$ is the Bessel function of the first kind and $H_m(x)$ is the Hankel function of the first kind, such that the scattered field in (2.5) clearly satisfies the radiation condition at infinity [3]. In order

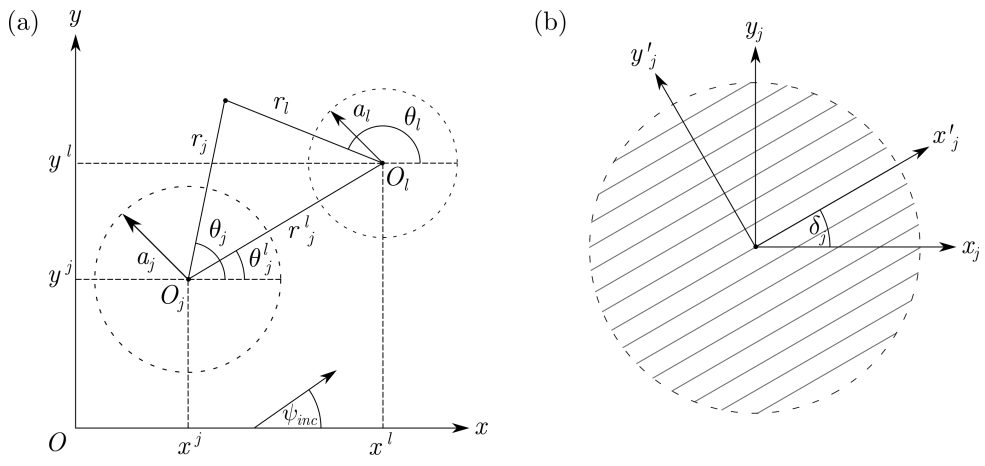


**Figure 2.** (a) Coordinate systems of cylinders $j$ and $l$ of radii $a_j$ and $a_l$ and the inter-cylinder coordinate system $(r^l_j, \theta^l_j)$. (b) Coordinate systems of the $j_{\text{th}}$ metacylinder, with plate array being merely illustrative and not a representation of the number of plates or spacing. Cylinder coordinates rotated through cylinder angle $\delta_j$ to primed plate array coordinates.

to proceed to a solution for the unknown scattering coefficients $b_{l,m}$ it is necessary to express the solution at any point in the exterior domain in terms of the coordinates of a single cylinder exclusively. To do so we use Graf's addition theorem [25] **9.1.79**, writing the total wavefield at any point in the vicinity of the metacylinder in terms of coordinates of the $j_{\text{th}}$ cylinder

$$K_z^{ext}(r_j,\theta_j) = e^{ik(x^j\cos(\psi_{inc})+y^j\sin(\psi_{inc}))}\sum_{m=-\infty}^{\infty} i^m J_m(k_\perp r_j)e^{im(\theta_j-\psi_{inc})}$$
$$+\sum_{m=-\infty}^{\infty} b_{j,m}H_m(k_\perp r_j)e^{im\theta_j}+\sum_{\substack{l=1\\ l\neq j}}^{N}\sum_{m=-\infty}^{\infty} b_{l,m}\sum_{q=-\infty}^{\infty} e^{i(m-q)\theta^l_j}H_{q-m}(k_\perp r^l_j)J_q(k_\perp r_j)e^{iq\theta_j}. \tag{2.6}$$

Here $(x^j, y^j)$ represents the location of the $j_{\text{th}}$ cylinder in global coordinates and $(r^l_j, \theta^l_j)$ refer to the inter-cylinder coordinates, representing the location of cylinder $l$ with respect to cylinder $j$. The incident wave has also been rewritten in terms of the coordinates of the $j_{\text{th}}$ cylinder, such that the total field is now expressed exclusively in terms of the coordinates $(r_j, \theta_j)$. It is straightforward to replace the plane-wave in (2.6) with a line-source of desired order; see Appendix B.

## (b) Metacylinder Medium

The metacylinder medium consists of a parallel array of closely-spaced thin vertical plates of infinite depth and decreasing length outwards, such that when viewed from above they form a cylinder of circular cross-section of radius $a_j$, where the subscript denotes the $j_{\text{th}}$ cylinder; see Fig. 2(b). The interior plate array is aligned at cylinder angle $\delta_j$ with respect to the $x$-axis, with $\delta_j \in [0, 2\pi)$. The homogenisation model of Porter describing these metacylinders assumes the ratio of plate array spacing, $d_p$, to length, $L$, has $d_p/L \ll 1$, and relies on expanding the governing Helmholtz equation in the small parameter $\epsilon = d_p/L$ to leading orders. For brevity we omit the derivation of the governing equation in the interior, and refer the reader to [17] or [19] for the derivation in full. The result of this expansion being that the metacylinder interior can be simply described as an effective medium that permits only forward and backward travelling waves to

propagate. The resultant governing equation in the interior of the $j_{\text{th}}$ metacylinder is of the form

$$\left(\frac{\partial^2}{\partial x_j'^2} + k_\perp'^2\right) K_{z,j}^{int} = 0 \quad \text{in} \quad r_j < a_j, \tag{2.7}$$

where $K_{z,j}^{int}$ refers to the interior solution and $r_j$ the local radial coordinate of the metacylinder, and $x_j'$ refers to the locally rotated cylinder axis i.e. $x_j = x_j' \cos(\delta_j)$. Here $k_\perp' = k_\perp(1 + i\nu)$ where $\nu$ represents damping and depends on the choice of interstitial material. Equation (2.7) permits solutions of the form

$$K_{z,j}^{int} = C_j(y_j')e^{ik_\perp' x_j'} + D_j(y_j')e^{-ik_\perp' x_j'}, \tag{2.8}$$

where the unknown coefficients $C_j(y_j')$, $D_j(y_j')$ describe the forward and backward travelling wave amplitudes. In order to solve for these coefficients, we look to the boundary of the object $r_j = a_j$ where $x_j' = a_j \cos(\theta_j - \delta_j)$, $y_j' = a_j \sin(\theta_j - \delta_j)$ and expand the coefficients in terms of Chebyshev polynomials:

$$\{C_j(y_j'), D_j(y_j')\} = \sum_{n=0}^{\infty} \{c_{j,n}, d_{j,n}\} T_n\left(\frac{y_j'}{a_j}\right) = \sum_{n=0}^{\infty} \{c_{j,n}, d_{j,n}\} \cos\left(n\left(\theta_j - \delta_j - \frac{\pi}{2}\right)\right). \tag{2.9}$$

Expressing the exponential terms in (2.8) in terms of the local radial coordinate and making use of the Jacobi-Anger expansion [26] (3.89), we arrive to an expression for the total internal wavefield at the boundary of the $j_{\text{th}}$ metacylinder

$$\begin{aligned} K_{z,j}^{int} = &\sum_{n=0}^{\infty} c_{j,n} \cos\left(n\left(\theta_j - \delta_j - \frac{\pi}{2}\right)\right) \sum_{m=-\infty}^{\infty} i^m J_m(k_\perp' r_j) e^{im(\theta_j - \delta_j)} \\ &+ \sum_{n=0}^{\infty} d_{j,n} \cos\left(n\left(\theta_j - \delta_j - \frac{\pi}{2}\right)\right) \sum_{m=-\infty}^{\infty} (-i)^m J_m(k_\perp' r_j) e^{im(\theta_j - \delta_j)}. \end{aligned} \tag{2.10}$$

It is necessary now to point out that this continuum model fails to converge at wavenumbers $k_\perp a_j \geq \pi/2$, a regime in which the metacylinder undergoes a continuum of resonance. Resonance occurs as an integer number of half-wavelengths circumnavigate the interstitial channels, causing large-amplitude wave propagation within the effective medium. At this wavenumber scale the assumption of separation of wavelength scales and plate separation scales breaks down [16], with the local wavenumber on the edge of the plate-array approaching infinity. Computations involving non-zero internal damping *do* converge, but not to the solution that would exist for an undamped continuum of plates. Henceforth then we are confined to the realm $k_\perp a_j < \pi/2$ in all computations, and set $\nu = 0$ unless otherwise specified.

## (c) Continuity Conditions

By replacing the internal cylinder material with that of a permeable effective medium we substitute the classical Neumann or Dirichlet type boundary conditions on the cylindrical surface with continuity of both the wavefield and flux. Across the boundary of the $j_{\text{th}}$ metacylinder,

$$K_{z,j}^{int} = K_z^{ext} \quad \text{at} \quad r_j = a_j, \tag{2.11}$$

$$\frac{\partial K_{z,j}^{int}}{\partial x_j'} \cos(\theta_j - \delta_j) = \frac{\partial K_z^{ext}}{\partial r_j} \quad \text{at} \quad r_j = a_j, \tag{2.12}$$

where the $\cos(\theta_j - \delta_j)$ term in (2.12) is necessary to describe the flux continuity at any point along the curved cylindrical boundary [18]. We carry out the substitution of the fields (2.6) and (2.10) into (2.11) and (2.12) in Appendix A.

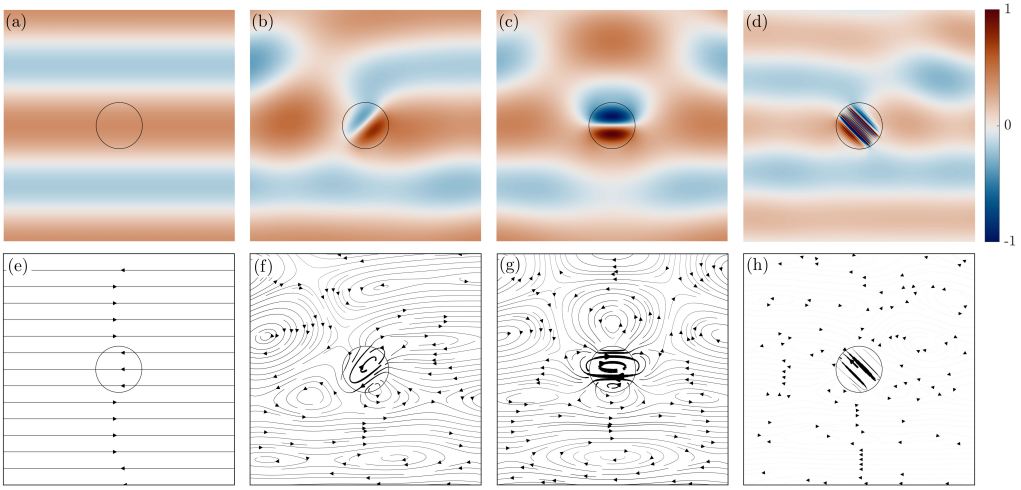


**Figure 3.** The scattering of a plane-wave of angle of incidence $\psi_{inc} = \pi/2$ by a single metacylinder at cylinder angle (a, e) $\delta = \pi/2$, $k_\perp a = 1.2$ (b, f) $\delta = \pi/4$, $k_\perp a = 1.2$, (c, g) $\delta = 0$, $k_\perp a = 1.2$ and (d, h) $\delta = -\pi/4$, $k_\perp a = \pi/2$. Panels (a)-(d) delineate the normalised magnetic field $H_z$ with colour depicting field strength, whereas panels (e)-(h) delineate the normalised electric field $\mathbf{E}$ with line-width depicting field strength. Computations carried out at truncation point (a)-(c) $M = 20$, $\nu = 0$ and (d) $M = 60$, $\nu = 10^{-3}$.

## (d) Scattering

The scattering of light by $N$ metacylinders has been reduced to a straightforward calculation of scattering coefficients, with a scattering matrix relating the unknowns of all cylinders $b_{l,m}$, $c_{l,n}$ and $d_{l,n}$ to the incident plane-wave or line-source at the boundary of the metacylinders. The system of equations is provided in Appendix B and follows readily from the continuity conditions of Appendix A. For an arrangement of $N$ metacylinders the incident and subsequent scattered fields are related by

$$\mathbf{TA} = \mathbf{Q}, \tag{2.13}$$

where $\mathbf{A}$ represents the vector of unknowns for all cylinders $l \in [1, N]$, $\mathbf{Q}$ the field due to the plane-wave or line-source at each cylinder and $\mathbf{T}$ the scattering matrix relating the two. The truncation point $M$ of the infinite multipole and Chebyshev expansions is chosen such that both the interior and exterior fields sufficiently converge. In this we are guided by the authors of [18] in choosing $M \geq 20$ for $k_\perp a_l = 1.3$, although good convergence is observed at as little as $M = 8$ for smaller wavenumbers and $M \geq 50$ is necessary as $k_\perp a_l \to \pi/2$.

In Fig. 3 we provide computations delineating the scattering of a plane-wave of incident angle $\psi_{\text{inc}} = \pi/2$ by a single metacylinder of radius $a_l = a$ in the global coordinate system. The transparency of the metamaterial to the plane-wave is apparent in panels 3(a, e) at which $\delta = \psi_{\text{inc}}$ such that the plane-wave is entirely undisturbed by the presence of the metacylinder. Upon rotation this picture changes, with panels depicting scattering by a metacylinder at (b, f) $\delta = \pi/4$, (c, g) $\delta = 0$ and (d, h) $\delta = -\pi/4$ respectively. In all cases, the maxima of magnetic and electric field strengths occur within the effective medium, within which the field strengths dwarf those of the exterior fields. Panels (d, h) delineate resonance occurring at $k_\perp a = \pi/2$ at which an integer number of wavelengths circumnavigate the interstitial channels, and it is at this point that the continuum model of Porter breaks down, failing to converge as the truncation point $M \to \infty$. In order to arrive to a converged solution it was necessary to use a damped wavenumber of $\nu = 10^{-3}$ such that the resonance has been dampened out.

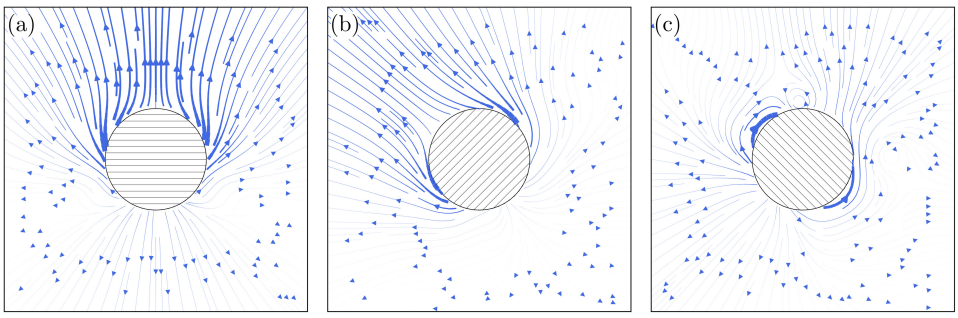


**Figure 4.** The normalised Poynting vector field corresponding to the scattered electric and magnetic fields of an incident plane-wave of angle $\psi_{inc} = \pi/2$. At wavenumber and cylinder angle (a) $k_\perp a = 1.2$, $\delta = 0$, (b) $k_\perp a = 1.3$, $\delta = \pi/4$ and (c) $k_\perp a = 1.4$, $\delta = -\pi/4$. Computations carried out at (a) $M = 20$, (b) $M = 30$ and (c) $M = 40$. Plates drawn in the disc are for illustrative purpose only.

The scattering of a plane-wave depicted in Figures 3 is complemented by the introduction of the Poynting vector, here used to illustrate the directional energy flux of the scattered fields $\mathbf{E}_s$ and $\mathbf{H}_s$ in the immediate vicinity of the metacylinder. For time-harmonic fields the Poynting vector is defined as

$$\mathbf{S} = \frac{1}{2}\mathbf{E}_s \times \mathbf{H}_s^*, \tag{2.14}$$

such that the time-averaged power flow is by definition $\langle \mathbf{S} \rangle = \mathrm{Re}\{\mathbf{S}\}$. Here $*$ denotes the complex conjugate. In Fig. 4 we provide the real part of the Poynting vector field normalised by the maximum in time-averaged power flow i.e. $\langle \mathbf{S} \rangle / \langle \mathbf{S} \rangle_{max}$ in the vicinity of the metacylinder at three different wavenumbers and cylinder angles. In all cases the power flow points predominantly along the direction perpendicular to the effective medium with minimal energy propagation along the $\delta$ direction. As the wavenumber approaches resonance, strong recirculation can be observed between the channel mouths, as in panel (c), illustrating how neighbouring channel amplitudes become inter-connected as the local wavenumber in the vicinity of the plate-array grows. The directionality of the scattered energy propagation has ramifications for the types of array-guided modes we will see in propagation along singly-periodic metagratings; we may expect that the maximal and minimal propagation along the structure to occur at $\delta = \pi/2$ and $\delta = 0$ respectively, on the grounds that we observe the maximal energy propagation occurring along the direction perpendicular to the plate array.

## 3. Infinite Metagrating

Noting the anisotropic scattering of wave energy, apparent in the Poynting vector field in the vicinity of the metacylinder (Fig. 4), we consider the scattering of a plane-wave by an infinite singly-periodic metagrating and retrieve the far-field reflection and transmission spectra as a function of cylinder angle $\delta$, see Fig. 1. For a plane-wave of angle $\psi_{\mathrm{inc}}$ incident on an infinite grating of metacylinders arranged periodically and of characteristic spacing $d$, uniform radius $a_j = a$ and uniform cylinder angle $\delta_j = \delta$, the field modulation along the grating is described by a simple phase shift on the field coefficients

$$b_{j,m} = e^{i\beta dj} b_{0,m} \tag{3.1}$$

for $j \in \mathbb{Z}$, where $\beta = k_\perp \cos(\psi_{inc})$ is the wavenumber component along the grating and $b_{0,m}$ is the $m_{\mathrm{th}}$ scattered field coefficient of the zeroth metacylinder. The scattered field in the vicinity of the $0_{th}$ metacylinder is discerned from (2.6) under consideration of the grating geometry where

$r_0^j = d|j|$ and $\theta_0^j = 0$ for $j \geq 0$ or $\theta_0^j = \pi$ for $j < 0$. Accordingly in $r_0 < d$

$$\begin{aligned} K_{z,s}^{ext}(r_0,\theta_0) &= \sum_{m\in\mathbb{Z}} b_{0,m} H_m(k_\perp r_0) e^{im\theta_0} \\ &+ \sum_{\substack{j\in\mathbb{Z}\\ j\neq 0}} e^{i\beta dj} \sum_{m\in\mathbb{Z}} b_{0,m} \sum_{q\in\mathbb{Z}} \mathrm{sgn}(j)^{m-q} H_{q-m}(k_\perp d|j|) J_q(k_\perp r_0) e^{iq\theta_0} \\ &= \sum_{m\in\mathbb{Z}} b_{0,m} H_m(k_\perp r_0) e^{im\theta_0} + \sum_{m\in\mathbb{Z}} b_{0,m} \sum_{q\in\mathbb{Z}} \sigma_{m-q}(\beta) J_q(k_\perp r_0) e^{iq\theta_0} \end{aligned} \tag{3.2}$$

where $K_{z,s}^{ext}$ denotes the scattered field in the exterior domain and

$$\sigma_n(\beta) = \sum_{j=1}^{\infty} H_n(k_\perp dj)((-1)^n e^{i\beta dj} + e^{-i\beta dj}) \tag{3.3}$$

is the lattice sum. Note that $\sigma_{-n} = (-1)^n \sigma_n$ such that we need only compute the lattice sums of order $n \geq 0$. By inspection of (A 1)-(A 2) it is clear that the equivalent continuity conditions on the zeroth metacylinder in the infinite grating are,

$$\begin{aligned} &i^p J_p(k_\perp a) e^{-ip\psi_{inc}} + b_p H_p(k_\perp a) + J_p(k_\perp a) \sum_{m\in\mathbb{Z}} b_m \sigma_{m-p}(\beta) \\ &= \frac{1}{2} e^{ip(\frac{\pi}{2}-\delta)} \sum_{n=0}^{\infty} (c_n(-1)^n + d_n(-1)^p)(J_{p-n}(k'_\perp a) + J_{p+n}(k'_\perp a)), \end{aligned} \tag{3.4}$$

$$\begin{aligned} &i^p J'_p(k_\perp a) e^{-ip\psi_{inc}} + b_p H'_p(k_\perp a) + J'_p(k_\perp a) \sum_{m\in\mathbb{Z}} b_m \sigma_{m-p}(\beta) \\ &= (1+i\nu)\frac{1}{2} e^{ip(\frac{\pi}{2}-\delta)} \sum_{n=0}^{\infty} (c_n(-1)^n + d_n(-1)^p)(J'_{p-n}(k'_\perp a) + J'_{p+n}(k'_\perp a)), \end{aligned} \tag{3.5}$$

where we have written $b_{0,m} = b_m$ etc. Together (3.4) and (3.5) form a system of equations for the plane-wave scattering by an infinite metagrating. However, in its current form the requisite sum (3.3) is slow to converge and is not suitable for computation. Twersky [21], referring to (3.3) as a Schlömilch series, derived an elementary function representation which is more amenable to computation and we provide this form in Appendix C in our notation. Essentially, the lattice sum (3.3) is recast as a sum over plane-waves of angle $\psi_m(\beta)$ for $m \in \mathbb{Z}$ where

$$\psi_m = \arccos\left(\frac{\beta_m}{k_\perp}\right) \quad \text{where} \quad \beta_m = \beta + \frac{2m\pi}{d}, \tag{3.6}$$

such that $\psi_0 \equiv \psi_{inc}$. When $|\beta_m| < k_\perp$ we say $m \in \mathcal{M}$ for which all $\psi_m$ are real and of value $0 < \psi_m < \pi$. Whereas when $|\beta_m| > k_\perp$, $\psi_m$ are now complex and one must use

$$\arccos(x) = \begin{cases} i\,\mathrm{arccosh}(x) & \text{if } x > 1, \quad (3.7a) \\ \pi - i\,\mathrm{arccosh}(-x) & \text{if } x < -1, \quad (3.7b) \end{cases}$$

where $\mathrm{arccosh}(x) = \ln(x + \sqrt{x^2-1})$ for $x > 1$; see [7,13]. The reflection and transmission coefficients are extracted from the expressions for the the far-field in $y < 0$ and $y > 0$ respectively, and are determined in the manner following Linton *et al.* [13] equations (2.13)-(2.16). This involves implementing the integral form of the Hankel function defining the outgoing waves into the expression for the scattered field on the right-hand-side of (2.5) and making use of the Poisson summation formula to obtain

$$K_{z,s}^{ext} = \sum_{m\in\mathbb{Z}} \frac{2e^{ik_\perp r\cos(\theta\mp\psi_m)}}{k_\perp d\sin(\psi_m)} \sum_{n\in\mathbb{Z}} (-i)^n b_n e^{\pm in\psi_m}, \tag{3.8}$$

where $\pm$ refers to the $y > 0$ and $y < 0$ regions respectively. The far-field is encapsulated by only those terms for which $|\beta_m| < k_\perp$ i.e. for real $\psi_m$ such that the far-field is composed of a set of

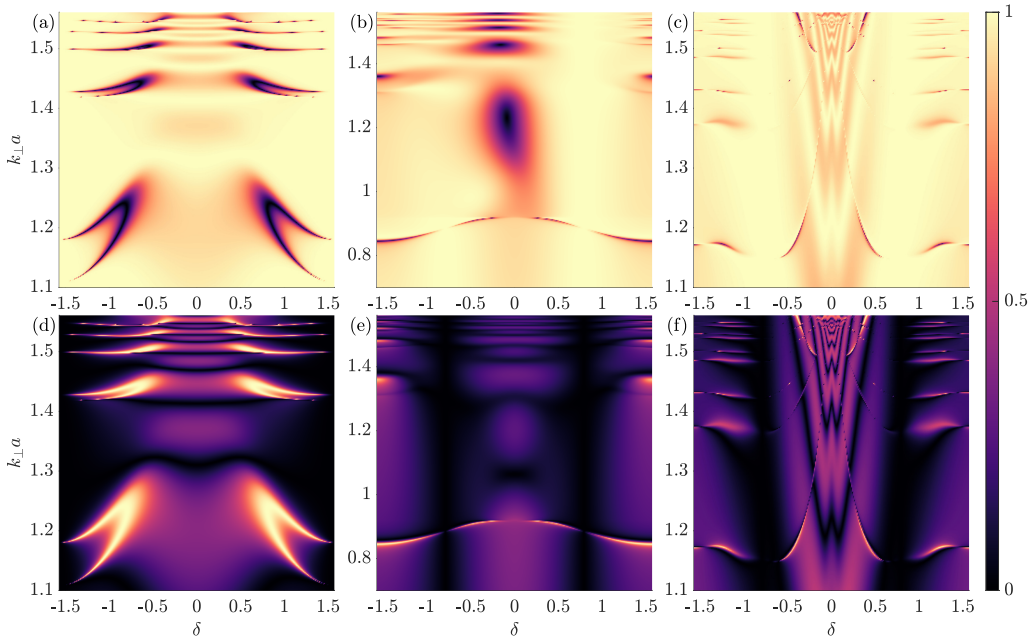


**Figure 5.** Phase-space portraits delineating $|\bar{T}_0|$ (top row) and $|\bar{R}_0|$ (bottom row) for which (a, b) $\psi_{\text{inc}} = \pi/2$ and $a = 0.25d$, (b, e) $\psi_{\text{inc}} = \pi/4$ and $a = 0.25d$ and (c, f) $\psi_{\text{inc}} = \pi/4$ and $a = 0.49d$. The self-similar features are reminiscent of the Hofstadter butterfly [27] that is generated by the angles $\delta$.

plane-waves of propagation directions $\theta = \pm\psi_m$ as $y \to \pm\infty$. Thus

$$K_{z,s}^{ext} \sim \sum_{m\in\mathcal{M}} \frac{2e^{ik_\perp r\cos(\theta\mp\psi_m)}}{k_\perp d\sin(\psi_m)} \sum_{n\in\mathbb{Z}} (-i)^n b_n e^{\pm in\psi_m} \quad \text{as} \quad y \to \pm\infty \tag{3.9}$$

where the reflection and transmission coefficients can be identified as

$$R_m = \frac{2}{k_\perp d\sin(\psi_m)} \sum_{n\in\mathbb{Z}} (-i)^n b_n e^{-in\psi_m}, \tag{3.10}$$

$$T_m = \delta_{0m} + \frac{2}{k_\perp d\sin(\psi_m)} \sum_{n\in\mathbb{Z}} (-i)^n b_n e^{+in\psi_m}, \tag{3.11}$$

for the diffraction orders $m \in \mathcal{M}$, where $\delta_{0m}$ accounts for the incident plane-wave. According to Achenbach *et al.* [22] equations (6.1)-(6.3) and later Linton and Evans [28], by considering the time-averaged net power flow through the fundamental cell, the reflection and transmission coefficients form the criterion

$$\sum_{m\in\mathcal{M}} \frac{t_m}{t_0}(|R_m|^2 + |T_m|^2) = 1 \quad \text{where} \quad t_m = \left(1 - \left(\frac{\beta_m}{k_\perp}\right)^2\right)^{\frac{1}{2}}. \tag{3.12}$$

Although this was originally derived under the assumption of a Neumann condition on the cylindrical boundary, we may omit the integral over the metacylinder surface by asserting that due to the permeability of the effective medium, integrating over the cell walls encapsulates the flow through the metacylinder. Thus (3.12) describes the conservation of energy of the metagrating as expressed by the coefficients denoting the reflected and transmitted mode energies in the far-field. As was pointed out in [29] however condition (3.12) implies that $R_m$ and $T_m$ do not represent the physical quantities of reflection and transmitted mode energy, but rather

coefficients that require rescaling by a 'normalising factor' $t_m/t_0$, to obtain

$$\bar{R}_m = \sqrt{\frac{t_m}{t_0}} R_m, \quad \bar{T}_m = \sqrt{\frac{t_m}{t_0}} T_m \tag{3.13}$$

that therefore satisfy

$$\sum_{m\in\mathcal{M}} (|\bar{R}_m|^2 + |\bar{T}_m|^2) = 1. \tag{3.14}$$

Equation (3.14) has been used to verify the correct computational implementation of the system formed by (3.4) and (3.5), and we observe sufficient convergence in computation at wavenumbers up to $k_\perp a = \pi/2$ for $M \geq 20$ for which (3.14) is satisfied to 9 s.f.

We are now in a position to determine the far-field scattering behaviour of the metagrating, and illustrate these results by providing portraits in phase-space of the rescaled coefficients (3.13) in Fig. 5. These phase portraits reveal the behaviour of the metagrating as both $\delta$ and $k_\perp a$ are varied, and therefore offer a more complete description of the scattering of wave energy. Beginning with Fig. 5(a, d), which respectively delineate $|\bar{T}_0|$ and $|\bar{R}_0|$ under $\psi_0 = \pi/2$ incidence, we provide the phase portrait in the space $\delta \in [-\pi/2, \pi/2]$ and $1.1 \leq k_\perp a < \pi/2$ (beneath which the wave undergoes little reflection, leaving the phase-space uniformly monochromatic) for a grating of uniform cylinder radius $a = 0.25d$. The immediate observation is that of symmetry about $\delta = 0$ as well as exact inversion between the portraits as the zeroth order mode is the only mode cut-on; this includes the expected result of transparency at $\delta = \pm\pi/2$, at which the metagrating permits perfect transmission at all wavenumbers. From panels (a, d) we also identify regions of perfect reflection $|\bar{R}_0| = 1$ that, to the authors' knowledge, do not occur for gratings of Neumann cylinders of any radius, cross-section or angle of incidence [22,28,31], with the exception being touching cylinders when $\psi_0 = \pi/2$ in Fig. 3 of [28]. In emphasising this result we take a horizontal slice of phase-space at $k_\perp a = 1.2$ over all $\delta$ and plot the reflection and transmission spectra in Fig. 6(a), making clear the points in the spectra at which there is perfect reflection. We plot an accompanying scattering computation illustrating perfect reflection in panel 6(b), for which the metagrating consists of $N = 101$ metacylinders of angle $\delta = 0.868$. At this cylinder angle and wavenumber there is no visible propagation of wave energy into the region above the metagrating.

In addition, these portraits reveal symmetry in $\delta$, and hence $\psi_0$, even at angles of incidence away from normal as long as the wavenumber of incidence is below that of the cut-on wavenumber for higher-order modes. In Fig. 5 panels (b, e) the phase portraits of $|\bar{T}_0|$ and $|\bar{R}_0|$ are provided for $\psi_0 = \pi/4$ incidence on a grating of $a = 0.25d$, in the region $\delta \in [-\pi/2, \pi/2]$ and $0.7 \leq k_\perp a < \pi/2$. The same symmetry about $\delta = 0$ as Fig. 5(a, d) is exhibited until the cut-on wavenumber is reached at $k_\perp a \approx 0.92$ at which the $m = -1$ modes are cut-on. By once again making a slice along $k_\perp a = 1.2$ and plotting the reflection and transmission spectra for all $\delta$ in panel 6(c), which now additionally features $|R_{-1}|$ and $|T_{-1}|$, we can see how mode energies of different order compete for dominance in the phase-space. The point labelled d lies at the maximum of the $m = -1$ transmission curve, with corresponding wavefield (d) demonstrating the 'reversed' transmission apparent in the total wavefield. This mode competitiveness accounts for the modulation of the wavefield in both the reflection and transmission regions, with the mode of largest magnitude dominating the image.

With the onset of higher-order modes spoiling the perfect symmetry in phase-space, we look to gratings of a larger radius such that at all wavenumbers in $k_\perp a < \pi/2$ lie below the cut-on wavenumber. A grating of $a = 0.49d$ (such that the cylinders are close to touching) retains its phase-space symmetry in this region, see Fig. 5(c, f), exhibiting perfect transmission at all wavenumbers at $\delta = -\psi_0$. To see how this is feasible, we refer the reader back to Fig. 4 and the observation therein that the scattered wave energy always points primarily along the direction perpendicular to $\delta$, even when the angle of incidence is co-linear with this direction as in Fig. 4(a). With this picture in mind, the non-intuitive result of perfect transmission when $\delta = -\psi_0$ becomes obvious; any wave energy not scattered by the metagrating continues to point along $\psi_0$, and

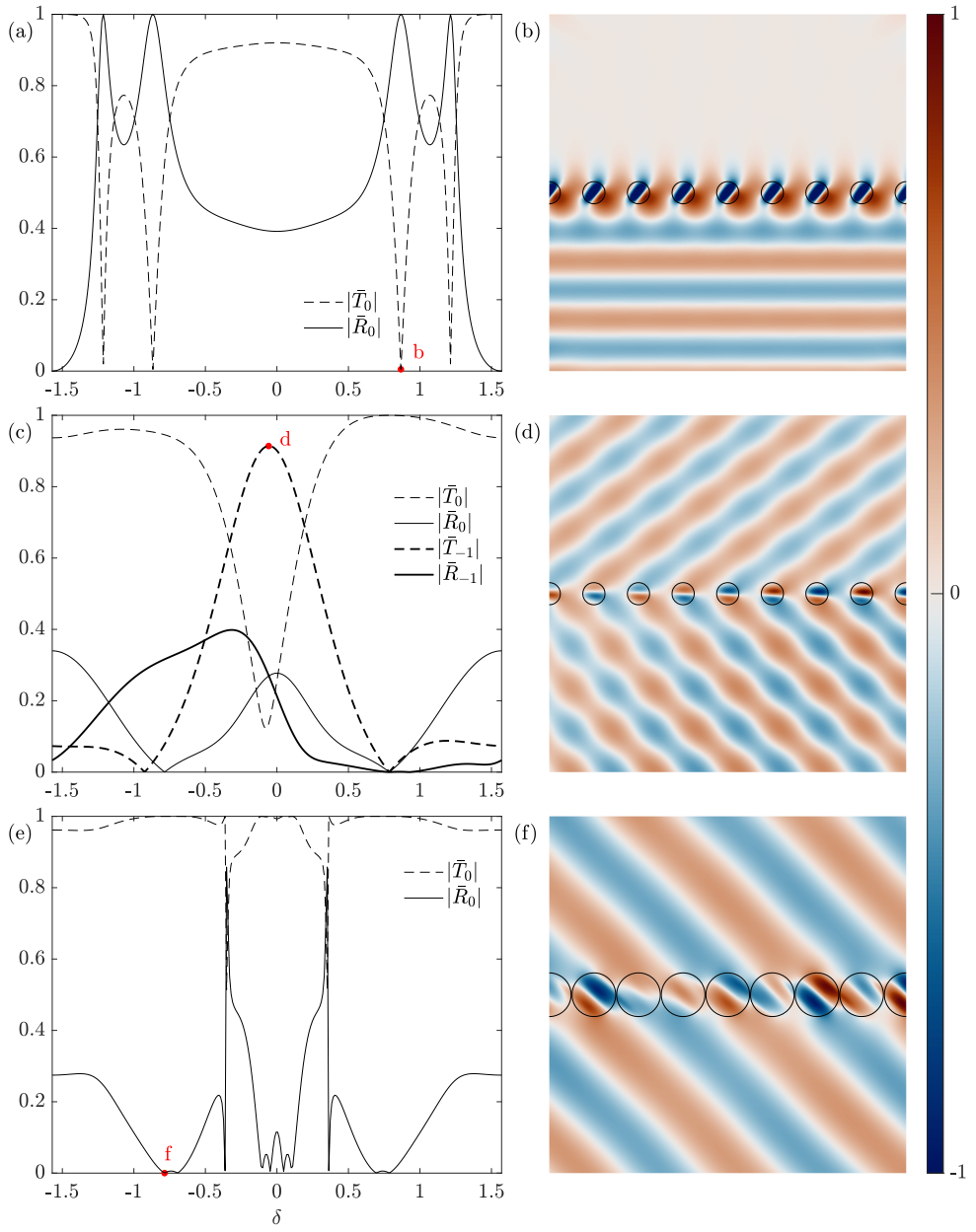


**Figure 6.** (a) Slice of phase-space at $k_\perp a = 1.2$ under $\psi_0 = \pi/2$ incidence on a grating of $a = 0.25d$. The wavefield (b), labelled in (a) at $\delta = 0.868$, is an example of perfect reflection of the incident plane-wave for which $|\bar{R}_0| = 1$. (c) Slice of phase-space at $k_\perp a = 1.2$ under $\psi_0 = \pi/4$ incidence on a grating of $a = 0.25d$. The wavefield (d), labelled in (c) at $\delta = -0.058$ delineates maximum transmission of the $|\bar{T}_{-1}|$ mode. (e) Slice of phase-space at $k_\perp a = 1.2$ under $\psi_0 = \pi/4$ incidence on a grating of $a = 0.49d$. The plane-wave undergoes perfect transmission at the point labelled (f), resembling a negative Goos-Hänchen shift [30] in the transmitted field.

any wave energy that is scattered by the metagrating points along the same direction. This perfect transmission at $\delta = -\psi_0$ can be observed in Fig. 6(e, f), and manifests as a negative translational shift in the transmitted field, or a Goos-Hänchen shift [30]. This can be likened to the waveshifting exhibited by Porter's singly-periodic plate array metamaterial [19], which allows

for exact translation of a plane-wave across the metamaterial without scattering. Similar Goos-Hänchen shifting can be observed along a grating of $a = 0.25d$ in Fig. 1(b), being imperfect due to competing higher-order modes.

The self-similar patterns of Fig. 5, evident as $k_\perp a \to \pi/2$, can be likened to those of [16] Fig. 2 on the transmission and reflection of waves by a metamaterial cavity sharing the same plate-array microstructure. As resonance is approached a higher truncation point $M$ is required to resolve the narrowing oscillatory behaviour of the reflection and transmission coefficients, with failure of convergence as $M \to \infty$ at and above resonance as in [16]. Interestingly, the phase portraits' symmetries share features to those seen in [32,33] on localised modes in linear clusters of scatterers. The symmetric pattern is known as the Hofstadter butterfly [27], and is strictly defined as a region in phase-space absent of bound modes. In our case these regions instead illustrate areas in phase-space absent of transmitted or reflected modes contributing to the far-field, and so we make this analogy between the two only lightly.

## 4. Tuneable Rayleigh-Bloch Modes

Thus far solutions satisfying the periodicity condition (3.1) have assumed that the wavenumber component along the grating $\beta$ depends on incident angle to the effect that $\beta < k_\perp$. If we relax this condition and insist $\beta > k_\perp$ then $\psi_0$ is complex by definition (3.7*a*) and the set $\mathcal{M} = \{\}$ such that there is no reflection or transmission in the directions perpendicular to the grating. This regime describes solutions that satisfy continuity conditions (2.11) and (2.12) in the absence of an incident wave, and are referred to as array-guided modes or Rayleigh-Bloch (RB) modes. The Rayleigh-Bloch modes of the metagrating manifest as the non-trivial solutions to the truncated system of equations formed by the following continuity conditions on the zeroth cylinder,

$$\begin{aligned} &- b_p H_p(k_\perp a) - J_p(k_\perp a) \sum_{m\in\mathbb{Z}} b_m \sigma_{m-p}(\beta) \\ &+ \frac{1}{2} e^{ip(\frac{\pi}{2}-\delta)} \sum_{n=0}^{\infty} (c_n(-1)^n + d_n(-1)^p)(J_{p-n}(k'_\perp a) + J_{p+n}(k'_\perp a)) = 0, \end{aligned} \tag{4.1}$$

$$\begin{aligned} &- b_p H'_p(k_\perp a) - J'_p(k_\perp a) \sum_{m\in\mathbb{Z}} b_m \sigma_{m-p}(\beta) \\ &+ (1+i\nu)\frac{1}{2} e^{ip(\frac{\pi}{2}-\delta)} \sum_{n=0}^{\infty} (c_n(-1)^n + d_n(-1)^p)(J'_{p-n}(k'_\perp a) + J'_{p+n}(k'_\perp a)) = 0, \end{aligned} \tag{4.2}$$

which follow from conditions (3.4) and (3.5). The non-trivial solutions correspond to the zeros of the resulting grating matrix $\mathbf{M}$ or the zeros of the matrix determinant, which is here complex and so we must solve for $|\det(\mathbf{M})| = 0$. Although using the determinant is not the most suitable method for finding the matrix zeros from a numerical point of view, we find that it is sufficient due to the small number of terms required by the continuum model for a converged solution. For guided modes on linear gratings of Neumann cylinders the wavenumber $k_\perp$ has been shown to be real [4,12], with an imaginary component being introduced only when a curvature is present in the periodic structure [5]. Thus we expect that the wavenumbers pertaining to RB modes for the metagrating should also be real, with the zeros of the grating matrix occurring along the $\mathrm{Re}\{k_\perp\}$ axis.

It is clear from the periodicity condition (3.1) that we need only consider the range $0 < \beta d \leq 2\pi$. Replacing $\beta d$ with $2\pi - \beta d$ (representing a wave propagating in the opposite direction) in (3.3) we have $\sigma_{m-p}(2\pi - \beta d) = (-1)^{p-m}\sigma_{m-p}(\beta d)$ and find that

$$k_\perp d(2\pi - \beta d) = k_\perp d(\beta d), \tag{4.3}$$

such that we need only consider the range $0 < \beta d \leq \pi$. Similarly, if one considers a wave travelling along a grating of equal and opposite cylinder angle $\delta \to -\delta$ then by symmetry of the geometry,

$$k_\perp d(-\delta) = k_\perp d(\delta). \tag{4.4}$$

The dispersion curves relating $\beta$ and $k_\perp$ for gratings of equal and opposite cylinder angle will therefore be indistinguishable, and we need only consider the range $0 \leq \delta \leq \pi/2$. In computation we find that metagratings host RB modes at discrete values of $k_\perp$ that satisfy

$$0 < k_\perp d < \beta d \leq \pi \tag{4.5}$$

for all $\beta d$ values, with the exception of the grating at cylinder angles at and approaching $\delta = 0$ for which no RB modes are found to exist. At all cylinder angles in the range $\pi/36 \lesssim \delta \leq \pi/2$ we identify a Rayleigh-Bloch wavenumber beneath the light-line $k_\perp = \beta$ for any $\beta$, and provide the dispersion curves relating $k_\perp d$ and $\beta d$ in the range $\beta d \in (0, \pi]$ in Fig. 7 for (a) various $\delta$ and (b) various $a$ (labelled). At any and all $\beta d$ values the corresponding RB wavenumber approaches the light-line in 7(a) as $\delta \to 0$, dovetailing with Fig. 4 in showing that as there is no energy propagation along the $\delta$ direction, no RB modes may propagate when $\delta = 0$. Similarly as $a \to 0$ we observe a shift upwards of the RB bands in 7(b), as was the case for arrays of circular cylinders [4] of Neumann boundary condition. In both panels 7(a) and 7(b) all dispersion curves flatten at the band-edge where $\beta d = \pi$, being standing wave solutions with energy localised to the vicinity of the metacylinders.

For arrays of impermeable circular cylinders Rayleigh-Bloch modes are conventionally distinguished by the symmetry of their waveform [4], being symmetric or antisymmetric about the grating axis by virtue of the symmetry of the geometry. This distinction arises from the signs of the Fourier coefficients of the scattered field, with denotation [13]

$$b_m = \begin{cases} (-1)^m b_{-m} & \text{Symmetric} \quad (4.6a) \\ -(-1)^m b_{-m} \text{ and } b_0 = 0 & \text{Antisymmetric.} \quad (4.6b) \end{cases}$$

In the context of the herein metacylinders however, a discussion on symmetry is only meaningful in the instance $\delta = \pi/2$ ($\delta = 0$ being symmetric in geometry but devoid of permissible RB propagation), with all other angles exhibiting RB modes that lack any describable symmetry about the grating axis. In the special case of $\delta = \pi/2$ then we find only symmetric solutions satisfying (4.6*a*), with no antisymmetric solutions permitted even at cylinder radii at and approaching $a = 0.5d$. This represents a clear distinction to gratings of impermeable cylinders, themselves having been shown to exhibit antisymmetric RB modes when the cylinder radius $a \gtrsim 0.403d$ [13]. This discrepancy likely arises from the greater connectedness between the neighbouring regions of the metagrating, with the interstitial channels between the plates being unable to host the requisite Dirichlet condition along $y = 0$ that is characteristic of antisymmetric modes [4]. Hence all RB solutions at cylinder angle $\delta = \pi/2$ are symmetric and satisfy (4.6*a*).

Conversely however there can be found an additional solution satisfying (4.5) for all $\beta d \gtrsim 3.019$ for $\delta = \pi/2$. These symmetric solutions lie along a flat-band at $k_\perp d \simeq 3.0172$ and are therefore a resonance of the metagrating, having a group velocity of zero. Naturally this distinguishes them from the RB modes which have a non-zero group velocity up to $\beta d = \pi$, at which the RB modes are standing wave solutions by virtue of the flattening of the dispersion bands towards the band-edge. In waveform the two permitted solutions are distinguished by the position of Dirichlet and Neumann conditions in the fundamental cell, with a Dirichlet condition bisecting the metacylinder being characteristic of RB modes, and a Neumann condition along the same line for grating resonances. These conditions rotate along with the effective medium, an effect illustrated in Fig. 9 in which we provide a gallery of RB and grating resonances at $\delta = \pi/2$ and $\delta = \pi/4$. The flat-band grating resonance rises to larger $k_\perp d$ like the Rayleigh-Bloch band as $\delta \to 0$ or $a/d \to 0$, always lying above the corresponding Rayleigh-Bloch band for any cylinder angle or radius. We provide both dispersion bands for a metagrating of radius $a = 0.25d$ in Fig. 8(a) at the same cylinder angles as in Fig. 7(a) (labelled).

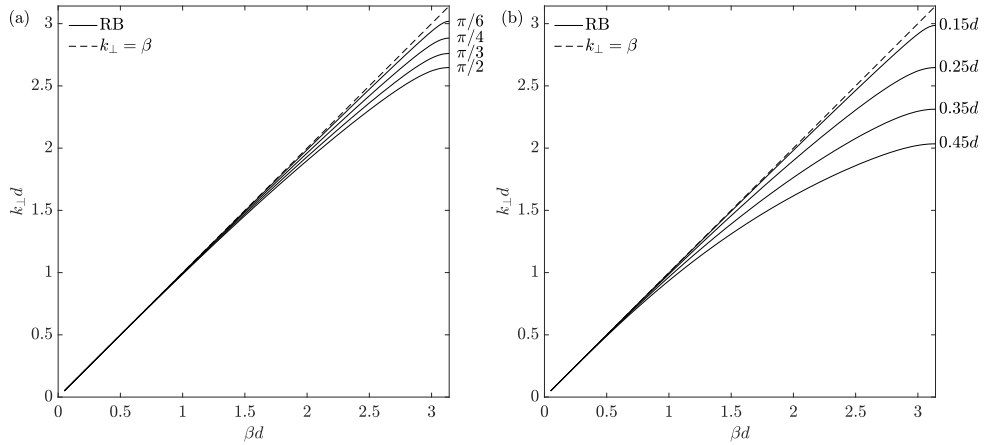


**Figure 7.** (a) RB dispersion bands belonging to a metagrating of radius $a = 0.25d$ at various cylinder angles $\delta$ (labelled). (b) RB dispersion bands belonging to a metagrating of $\delta = \pi/2$ at various radii (labelled).

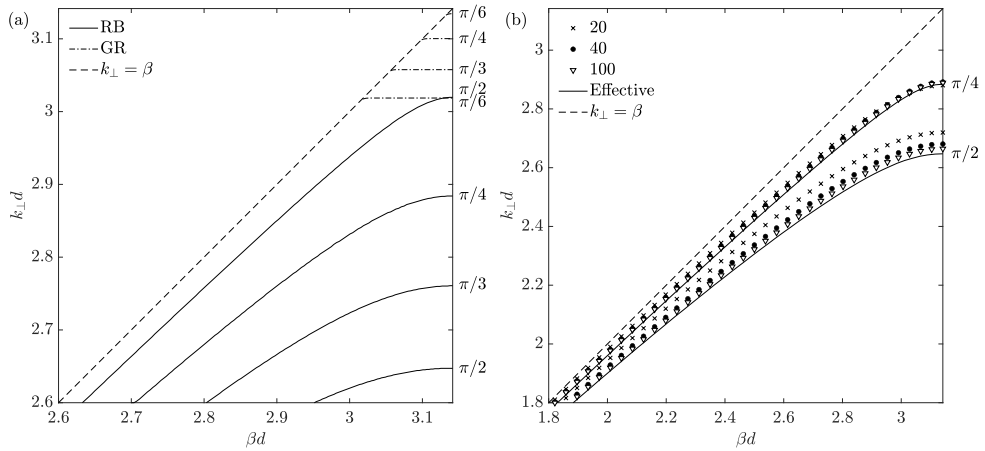


**Figure 8.** (a) Zoom-in of RB bands for $\beta d \in [2.6, \pi]$ with neighbouring grating resonances labelled by $\delta$ for a metagrating of uniform radius $a = 0.25d$. (b) Finite element computations (labelled with plate number) in comparison with the effective medium at two cylinder angles (labelled).

We now check that the solutions computed by the above RB theory for the effective model translate into RB modes hosted by a metagrating of finite plate number and spacing. We make a comparison to a metagrating modelled with finite element method (FEM) via software COMSOL Multiphysics, of constituent metacylinders of a finite number of plates, plate thickness and interstitial spacing. RB solutions are then computed by inserting a Bloch condition on the walls of the fundamental cell and performing a scan through wavenumber space, with the resulting predicted RB wavenumbers provided in Fig. 8(b), being the discrete sets of points superposed atop the continuous dispersion bands of the continuum model. The finite element computations are found to converge to those of the continuum model as the number of plates is increased, with solutions at smaller cylinder angle converging to the continuum model with a smaller number of plates than those of larger cylinder angle. The discrepancy between the FEM and the continuum model computations is largest towards the band-edge, with all FEM computations converging to one-another and the continuum model at smaller wavenumber. The close resemblance of the two methods validates the approximation of the metamaterial cylinder with the continuum model of Porter, and this confirmation is equivalently carried out by Zheng *et al.* through comparison of

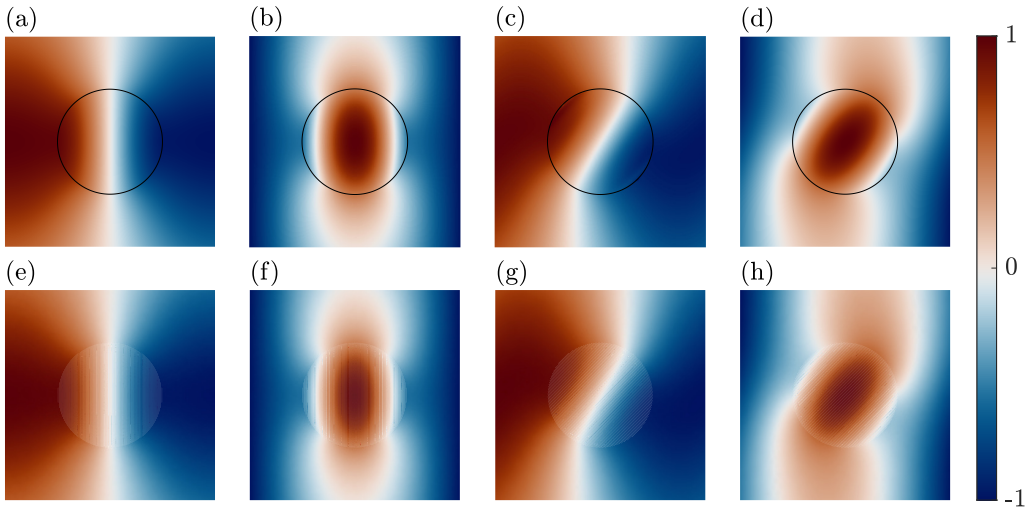


**Figure 9.** (a)-(d) Nullspace calculations corresponding to standing waves hosted by a metagrating of uniform $a = 0.25d$. (a) RB mode at $k_\perp d = 2.6748$ and $\beta d = \pi$ along a grating of $\delta = \pi/2$, paired with (b) a grating resonance along the flat-band at $k_\perp d = 3.0172$. Similarly (c, d) RB mode and grating resonance at (c) $k_\perp d = 2.8841$ and $\beta d = \pi$ and (d) $k_\perp d = 3.0996$ along a grating of cylinder angle $\delta = \pi/4$. (e)-(h) FEM calculations corresponding to standing waves hosted by a metagrating of uniform $a = 0.25d$, with metacylinders consisting of 100 evenly spaced plates. Wavenumbers $\beta d$ equalling those of (a)-(d).

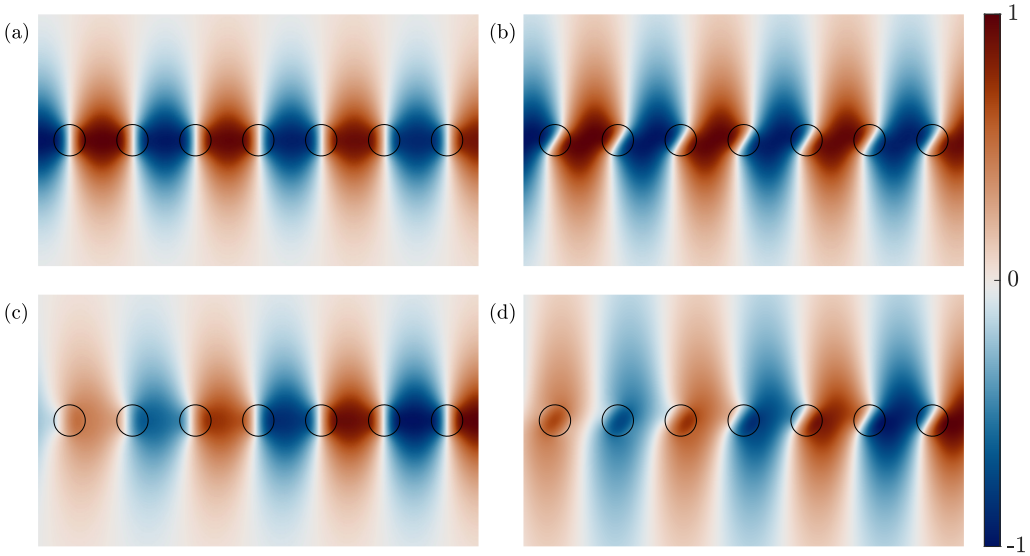


**Figure 10.** Standing (a, b) and propagating (c, d) RB modes along a grating of $a = 0.25d$, excited in a scattering simulation via a monopole line-source of wavenumbers (a) $k_\perp d = 2.6748$, $\delta = \pi/2$ and (b) $k_\perp d = 2.8841$, $\delta = \pi/4$, (c) $k_\perp d = 2.5993$, $\delta = \pi/2$ and (d) $k_\perp d = 2.7974$, $\delta = \pi/4$.

scattered wavefields [18]. Like Zheng, we point out that the continuum model is advantageous in that it offers a highly efficient method for the computation of wave scattering, and now additionally in the computation of the non-trivial solutions belonging to the grating.

In Fig. 9(a)-(d) we provide several Nullspace calculations of the fundamental grating cell corresponding to standing wave solutions hosted by the grating, taken at the band-edges of Figs. 7 and 8. Figure. 9(a) depicts the RB wavefield at the band-edge of the $\delta = \pi/2$ curve of Fig. 7(a), and can be distinguished from the neighbouring grating resonance of 9(b) by the discrepancy in the waveforms between the two; the RB mode having a characteristic Dirichlet condition bisecting the metacylinder and the grating resonance a characteristic Neumann condition along the same line. This remains the case in panels (c) and (d), which in turn depict an RB modes and a grating resonance at $\delta = \pi/4$. This illustrates the fact that solutions (a, c), and similarly (b, d), of equal wavenumber $\beta d$, are equivalent solutions under rotation. These Nullspace calculations should be compared to the neighbouring panels (e)-(h) which depict waveforms in the fundamental grating cell as calculated using a FEM implementation in COMSOL Multiphysics. Metacylinders consisting of 100 plates of thickness $0.0005$d and interstitial spacing $0.0045$d are shown to host identical array-guided solutions, being of equal $\beta d$ to those of panels (a)-(d).

Lastly, we demonstrate the excitation of RB modes in truncated metagratings in Fig. 10, retrieved by following the method set out in [13] of exciting RB modes along a finite grating by placing a monopole line-source of RB wavenumber at one end of the array and performing a scattering computation. We plot these scattered fields about the centroid of a grating of $N = 201$ metacylinders for gratings of (a, c) $\delta = \pi/2$ and (b, d) $\delta = \pi/4$. The close resemblance between the nullspace solutions of Fig. 9(a, c) to the scattered fields of Fig. 10(a, b) reaffirms that the RB theory is accurate in finding the array-guided modes, and that these modes are readily tuned through rotation of the uniform cylinder angle.

## 5. Conclusion

To summarise, we have developed the grating theory necessary to describe the scattering and guiding of light by an infinite metagrating of uniform cylinder angle and radius. Painting portraits in phase-space has revealed symmetries reminiscent of the Hofstadter butterfly, which here depicts regions of zero reflected or transmitted mode energies. Both the transparency to, and perfect reflection of, an incident plane-wave by a linear arrangement of non-touching scatterers are results that, to the authors' knowledge, cannot be found in the existing literature on singly-periodic gratings of two-dimensional scatterers [22,28,29,31]. We have also shown how the symmetry in phase-space manifests as a negative Goos-Hänchen shift in the transmitted field when $\delta = -\psi_{\text{inc}}$. Additionally, we have found that the metagrating hosts exclusively symmetric RB modes at all cylinder radii, with the dispersion of the RB modes contingent on the choice of both the uniform cylinder angle and radius. We have found that RB modes exist for all $0 < \beta d \leq \pi$, with the RB bands approaching the light-line as $\delta \to 0$ or $a \to 0$. Our RB theory has been shown to be in good agreement with FEM calculations, with RB wavenumbers as calculated by our FEM implementation approaching those of the continuum model as the number of plates inside a metacylinder is increased from 20 to 100; the smaller the $\delta$, the fewer number of plates required to reach a convergence of FEM to RB theory. Grating resonances have also been found to exist along flat-bands in the band scheme at wavenumbers above those of the Rayleigh-Bloch bands. The two permissible solutions are distinguished by the swapping of a Neumann or Dirichlet condition in the fundamental cell.

We remark that in both the scattering and guiding of waves, the key variable in determining the wave interaction is the cylinder angle. Through uniform rotation of the constituent metacylinders it is possible to bring about all of the aforementioned wave interactions, and this bears testament to our claim that the metagrating behaves as a tuneable surface. Indeed, the metagrating has the ability to host array-guided modes in a wide region of wavenumber space, as well as permit the antipodal phenomena of perfect transmission and perfect reflection, through just uniform rotation. This makes the metagrating considerably advantageous over gratings of impermeable cylinders that have no such degree of freedom, conventionally relying on altering the geometry itself to bring about novel wave effects. As the mathematical framework here is not unique to light, we foresee that metagratings in acoustics and water waves will exhibit analogous results.

Data Accessibility. The codes and data sets supporting this article have been uploaded as part of the supplementary material.

Authors' Contributions. **H.J. Putley:** Conceptualization, Formal Analysis, Methodology, Software, Visualization, Writing - original draft, Writing - review & editing. **S. Guenneau:** Conceptualization, Formal Analysis, Software, Validation, Visualization, Writing - review & editing. **R. Porter:** Conceptualization, Formal Analysis, Methodology, Writing - review & editing. **R.V. Craster:** Methodology, Supervision, Resources, Conceptualization, Writing - review & editing.

Competing Interests. The authors declare that they have no known competing financial interests or personal relationships that could have appeared to influence the work reported in this paper.

Funding. H.J. Putley is grateful for EPSRC (UK) funding provided through the Centre for Doctoral Training "Fluid Dynamics Across Scales" Programme grant no. EP/L016230/1. R.V. Craster received funding from the European Union's Horizon 2020 FET Open programme under grant agreement 863179 Boheme. H.J. Putley and R.V. Craster thank QinetiQ Ltd for discussions and the provision of an EPSRC Industrial CASE award that funded the primary author. R. Porter is grateful for the support from the EPSRC Grant No. EP/V04740X/1. S. Guenneau is grateful for the funding provided by the EPSRC Grant No. EP/T002654/1

Acknowledgements. Thanks is given to Professor Chris Linton of Loughborough University for his correspondence on the determination of the singly-periodic lattice sums.

# Appendices

## A. Continuity of Interior and Exterior Fields

Substitution of the interior (2.10) and exterior (2.6) fields into conditions (2.11) and (2.12) describes the continuity of the field and flux at any point $(a_j, \theta_j)$. Multiplying by $e^{-ip\theta_j}$ and integrating over $\theta_j \in [0, 2\pi]$ yields the following conditions over the metacylinder boundary,

$$\begin{aligned} &e^{ik(x^j\cos(\psi_{inc})+y^j\sin(\psi_{inc}))}i^pJ_p(k_\perp a_j)e^{-ip\psi_{inc}} \\ &+b_{j,p}H_p(k_\perp a_j)+\sum_{\substack{l=1\\l\neq j}}^{N}\sum_{m=-\infty}^{\infty}b_{l,m}e^{i(m-p)\theta_j^l}H_{p-m}(k_\perp r_j^l)J_p(k_\perp a_j) \\ &=\frac{1}{2}e^{ip(\frac{\pi}{2}-\delta_j)}\sum_{n=0}^{\infty}(c_{j,n}(-1)^n+d_{j,n}(-1)^p)(J_{p-n}(k'_\perp a_j)+J_{p+n}(k'_\perp a_j)), \end{aligned} \tag{A 1}$$

$$\begin{aligned} &e^{ik(x^j\cos(\psi_{inc})+y^j\sin(\psi_{inc}))}i^pJ'_p(k_\perp a_j)e^{-ip\psi_{inc}} \\ &+b_{j,p}H'_p(k_\perp a_j)+\sum_{\substack{l=1\\l\neq j}}^{N}\sum_{m=-\infty}^{\infty}b_{l,m}e^{i(m-p)\theta_j^l}H_{p-m}(k_\perp r_j^l)J'_p(k_\perp a_j) \\ &=(1+i\nu)\frac{1}{2}e^{ip(\frac{\pi}{2}-\delta_j)}\sum_{n=0}^{\infty}(c_{j,n}(-1)^n+d_{j,n}(-1)^p)(J'_{p-n}(k'_\perp a_j)+J'_{p+n}(k'_\perp a_j)), \end{aligned} \tag{A 2}$$

where the $'$ denotes the derivative of a Bessel function with respect to its argument. The flux condition (A 2) makes use of Bessel function identities for the derivatives on the right-hand-side.

## B. Scattering Matrix

Combining together conditions (A 1) and (A 2) allows us to solve for the unknown interior $c_{l,n}$, $d_{l,n}$ and exterior $b_{l,m}$ scattering coefficients for all cylinders $l \in [1, N]$. Indeed, by placing both the interior and exterior field terms on the left-hand-side and the plane-wave on the right-hand-side we arrive to the following system of equations describing the multiple scattering between all

objects,

$$\mathbf{TA} = \mathbf{Q} \tag{B 1}$$

where

$$\mathbf{T} = \left(\begin{array}{cccc|cccc|cccc} \mathbf{H}_1 & \mathbf{P}_{1,2} & \cdots & \mathbf{P}_{1,N} & \mathbf{C}_1 & \mathbf{0} & \cdots & \mathbf{0} & \mathbf{D}_1 & \mathbf{0} & \cdots & \mathbf{0} \\ \mathbf{P}_{2,1} & \mathbf{H}_2 & \cdots & \mathbf{P}_{2,N} & \mathbf{0} & \mathbf{C}_2 & \cdots & \mathbf{0} & \mathbf{0} & \mathbf{D}_2 & \cdots & \mathbf{0} \\ \vdots & \vdots & \ddots & \vdots & \vdots & \vdots & \ddots & \vdots & \vdots & \vdots & \ddots & \vdots \\ \mathbf{P}_{N,1} & \mathbf{P}_{N,2} & \cdots & \mathbf{H}_N & \mathbf{0} & \mathbf{0} & \cdots & \mathbf{C}_N & \mathbf{0} & \mathbf{0} & \cdots & \mathbf{D}_N \\ \hline \mathbf{H}'_1 & \mathbf{P}'_{1,2} & \cdots & \mathbf{P}'_{1,N} & \mathbf{C}'_1 & \mathbf{0} & \cdots & \mathbf{0} & \mathbf{D}'_1 & \mathbf{0} & \cdots & \mathbf{0} \\ \mathbf{P}'_{2,1} & \mathbf{H}'_2 & \cdots & \mathbf{P}'_{2,N} & \mathbf{0} & \mathbf{C}'_2 & \cdots & \mathbf{0} & \mathbf{0} & \mathbf{D}'_2 & \cdots & \mathbf{0} \\ \vdots & \vdots & \ddots & \vdots & \vdots & \vdots & \ddots & \vdots & \vdots & \vdots & \ddots & \vdots \\ \mathbf{P}'_{N,1} & \mathbf{P}'_{N,2} & \cdots & \mathbf{H}'_N & \mathbf{0} & \mathbf{0} & \cdots & \mathbf{C}'_N & \mathbf{0} & \mathbf{0} & \cdots & \mathbf{D}'_N \end{array}\right) \tag{B 2}$$

and $\mathbf{A} = (\mathbf{b}_1, \ldots, \mathbf{b}_N, \mathbf{c}_1, \ldots, \mathbf{c}_N, \mathbf{d}_1, \ldots, \mathbf{d}_N)^{\mathrm{T}}$, $\mathbf{Q} = (\mathbf{Q}_1, \ldots, \mathbf{Q}_N, \mathbf{Q}'_1, \ldots, \mathbf{Q}'_N)^{\mathrm{T}}$. The top half of $\mathbf{T}$ describes the field continuity and the bottom half the flux continuity. For computations we truncate the infinite Multipole and Chebyshev expansions such that they are of size $m, p \in [-M-1, M]$ and $n \in [0, M]$ respectively for some value $M$ which is chosen depending on the normalised wavenumber $k_\perp a$. Accordingly the matrix $\mathbf{S}$ is a square matrix of size $N(4M+4)$ rows and columns, with submatrices of the form

$$H_{j,p,m} = -\delta_{pm} H_p(k_\perp a_j), \tag{B 3}$$

$$P_{j,l,p,m} = -e^{i(m-p)\theta_j^l} H_{p-m}(k_\perp r_j^l) J_p(k_\perp a_j), \tag{B 4}$$

$$C_{j,p,n} = \frac{1}{2} e^{ip(\frac{\pi}{2}-\delta_j)} (-1)^n (J_{p-n}(k'_\perp a_j) + J_{p+n}(k'_\perp a_j)), \tag{B 5}$$

$$D_{j,p,n} = \frac{1}{2} e^{ip(\frac{\pi}{2}-\delta_j)} (-1)^p (J_{p-n}(k'_\perp a_j) + J_{p+n}(k'_\perp a_j)), \tag{B 6}$$

where $P_{j,l,p,m}$ refers to the $pm_{\mathrm{th}}$ element of the matrix $\mathbf{P}_{j,l}$ describing the scattered field due to cylinder $l$ at the boundary of cylinder $j$. Similarly $C_{j,p,n}$ and $D_{j,p,n}$ are the $pn_{\mathrm{th}}$ elements of the matrices $\mathbf{C}_j$ and $\mathbf{D}_j$ describing the interior field of metacylinder $j$ as a function of the cylinder angle $\delta_j$. The forms of the primed submatrices within $\mathbf{T}$ are readily found by cross-inspection between (B 3)-(B 6) and (A 1)-(A 2), being functions of the Bessel function derivatives. Each metacylinder vector of scattering coefficients is of the form $\mathbf{b}_l = (b_{l,-M-1}, \ldots, b_{l,M})$, $\mathbf{c}_j = (c_{j,0}, \ldots, c_{j,N})$ and $\mathbf{d}_j = (d_{j,0}, \ldots, d_{j,N})$. Lastly, each plane-wave vector $\mathbf{Q}_j$ describes the incident field at the boundary of cylinder $j$, where

$$\{Q_{j,p}, Q'_{j,p}\} = e^{ik(x^j \cos(\psi_{inc}) + y^j \sin(\psi_{inc}))} i^p \{J_p(k_\perp a_j), J'_p(k_\perp a_j)\} e^{-ip\psi_{inc}}, \tag{B 7}$$

Alternatively the above plane-wave can be replaced by a vector describing a line-source of form

$$\{Q_{j,p}, Q'_{j,p}\} = -\frac{1}{4i} e^{i(o-p)\theta_j^s} H_{p-o}(k_\perp r_j^s) \{J_p(k_\perp a_j), J'_p(k_\perp a_j)\}, \tag{B 8}$$

of some chosen order $o$ and relative source position $(r_j^s, \theta_j^s)$ to the $j_{\mathrm{th}}$ cylinder.

## C. Elementary Function Representation of Schlömilch Series

Twersky [21] and later Linton [7] showed that the one-dimensional lattice sums of type (3.3) can be written in the following rapidly convergent form:

$$\sigma_{2n} = 2(-1)^n \sum_{m\in\mathbb{Z}} \frac{e^{i2n\mathrm{sgn}(m)\psi_m}}{k_\perp d\sin(\psi_m)} + \frac{i}{\pi}\sum_{m=0}^{n} \frac{(-1)^m 2^{2m}(n+m-1)!}{(2m)!(n-m)!}\left(\frac{2\pi}{k_\perp d}\right)^{2m} B_{2m}\left(\frac{\beta d}{2\pi}\right) \tag{C 1}$$

$$\sigma_{2n-1} = 2(-1)^n i \sum_{m\in\mathbb{Z}} \frac{e^{i(2n-1)\mathrm{sgn}(m)\psi_m}}{k_\perp d\sin(\psi_m)} + \frac{2}{\pi}\sum_{m=0}^{n-1} \frac{(-1)^m 2^{2m}(n+m-1)!}{(2m+1)!(n-m-1)!}\left(\frac{2\pi}{k_\perp d}\right)^{2m+1} B_{2m+1}\left(\frac{\beta d}{2\pi}\right) \tag{C 2}$$

for $n \geq 1$ and

$$\sigma_0 = -1 - \frac{2i}{\pi}\left(C + \ln\left(\frac{k_\perp d}{4\pi}\right)\right) + \frac{2}{k_\perp d\sin(\psi_0)} + \sum_{\substack{m\in\mathbb{Z}\\ m\neq 0}} \left(\frac{2}{k_\perp d\sin(\psi_m)} + \frac{i}{|m|\pi}\right) \tag{C 3}$$

for $n = 0$. Here $B_m(x)$ refers to the Bernoulli polynomial and can be written as a finite sum, see [34] **9.620**, and $C$ is Euler's constant.

## References


1. Guenneau S, Poulton C, Movchan A. 2003 Oblique propagation of electromagnetic and elastic waves for an array of cylindrical fibres. *Proceedings of the Royal Society of London. Series A: Mathematical, Physical and Engineering Sciences* **459**, 2215–2263.
2. White T, Kuhlmey B, McPhedran R, Maystre D, Renversez G, De Sterke CM, Botten L. 2002 Multipole method for microstructured optical fibers. I. Formulation. *JOSA B* **19**, 2322–2330.
3. Yasumoto K. 2018 Chapter 1. In *Electromagnetic theory and applications for photonic crystals,*. CRC press.
4. Evans D, Porter R. 1999 Trapping and near-trapping by arrays of cylinders in waves. *Journal of Engineering Mathematics* **35**, 149–179.
5. Maling B, Craster R. 2016 Whispering Bloch modes. *Proceedings of the Royal Society A: Mathematical, Physical and Engineering Sciences* **472**, 20160103.
6. Kavaklioglu Ö. 2002 On Schlömilch series representation for the transverse electric multiple scattering by an infinite grating of insulating dielectric circular cylinders at oblique incidence. *Journal of Physics A: Mathematical and General* **35**, 2229.
7. Linton C. 2006 Schlömilch series that arise in diffraction theory and their efficient computation. *Journal of Physics A: Mathematical and General* **39**, 3325.
8. Zalipaev V, Movchan A, Poulton C, McPhedran R. 2002 Elastic waves and homogenization in oblique periodic structures. *Proceedings of the Royal Society of London. Series A: Mathematical, Physical and Engineering Sciences* **458**, 1887–1912.
9. Moreno E, Erni D, Hafner C. 2002 Modeling of discontinuities in photonic crystal waveguides with the multiple multipole method. *Physical Review E* **66**, 036618.
10. Evans D, Porter R. 1997 Near-trapping of waves by circular arrays of vertical cylinders. *Applied Ocean Research* **19**, 83–99.
11. Porter R, Evans D. 1999 Rayleigh–Bloch surface waves along periodic gratings and their connection with trapped modes in waveguides. *Journal of Fluid Mechanics* **386**, 233–258.
12. McIver P, Linton C, McIver M. 1998 Construction of trapped modes for wave guides and diffraction gratings. *Proceedings of the Royal Society of London. Series A: Mathematical, Physical and Engineering Sciences* **454**, 2593–2616.
13. Linton CM, Porter R, Thompson I. 2007 Scattering by a semi-infinite periodic array and the excitation of surface waves. *SIAM Journal on Applied Mathematics* **67**, 1233–1258.

14. Linton C, McIver M. 2002 The existence of Rayleigh–Bloch surface waves. *Journal of Fluid Mechanics* **470**, 85–90.
15. Bonnet-Bendhia AS, Starling F. 1994 Guided waves by electromagnetic gratings and non-uniqueness examples for the diffraction problem. *Mathematical Methods in the Applied Sciences* **17**, 305–338.
16. Jan AU, Porter R. 2018 Transmission and absorption in a waveguide with a metamaterial cavity. *The Journal of the Acoustical Society of America* **144**, 3172–3180.
17. Porter R. 2018 Plate arrays as a water wave metamaterial. In *33rd International Workshop on Water Waves and Floating Bodies, Guidel-Plages, France* pp. 1–4.
18. Zheng S, Porter R, Greaves D. 2020 Wave scattering by an array of metamaterial cylinders. *Journal of Fluid Mechanics* **903**.
19. Porter R. 2021 Plate arrays as a perfectly-transmitting negative-refraction metamaterial. *Wave Motion* **100**, 102673.
20. Porter R, Zheng S, Liang H. 2022 Scattering of surface waves by a vertical truncated structured cylinder. *Proceedings of the Royal Society A* **478**, 20210824.
21. Twersky V. 1961 Elementary function representations of Schlömilch series. *Archive for Rational Mechanics and Analysis* **8**, 323–332.
22. Achenbach J, Lu YC, Kitahara M. 1988 3-D reflection and transmission of sound by an array of rods. *Journal of sound and vibration* **125**, 463–476.
23. Poulton C, Guenneau S, Movchan A. 2004 Noncommuting limits and effective properties for oblique propagation of electromagnetic waves through an array of aligned fibres. *Physical Review B* **69**, 195112.
24. Wijngaard W. 1973 Guided normal modes of two parallel circular dielectric rods. *JOSA* **63**, 944–950.
25. Abramowitz M, Stegun IA. 1964 *Handbook of mathematical functions*. Dover Publications, New York.
26. Colton DL, Kress R, Kress R. 2013 *Inverse acoustic and electromagnetic scattering theory* vol. 93. Springer third edition.
27. Hofstadter DR. 1976 Energy levels and wave functions of Bloch electrons in rational and irrational magnetic fields. *Physical review B* **14**, 2239.
28. Linton C, Evans D. 1993 The interaction of waves with a row of circular cylinders. *Journal of Fluid Mechanics* **251**, 687–708.
29. Lynott GM, Andrew V, Abrahams ID, Simon MJ, Parnell WJ, Assier RC. 2019 Acoustic scattering from a one-dimensional array; Tail-end asymptotics for efficient evaluation of the quasi-periodic Green's function. *Wave Motion* **89**, 232–244.
30. Goos F, Hänchen H. 1947 A new and fundamental experiment on total reflection. *Ann. Phys.(Leipzig)* **1**, 333–346.
31. Evans D, Porter R, Chaplin J. 2018 Extraordinary transmission past cylinders in channels. *Proceedings of the 33rd International Workshop on Water Waves & Floating Bodies, Guidel-Plages, France*.
32. Apigo DJ, Qian K, Prodan C, Prodan E. 2018 Topological edge modes by smart patterning. *Physical Review Materials* **2**, 124203.
33. Martí-Sabaté M, Torrent D. 2021 Edge modes for flexural waves in quasi-periodic linear arrays of scatterers. *APL Materials* **9**, 081107.
34. Gradshteyn IS, Ryzhik IM. 2007 *Table of Integrals, Series, and Products*. Academic press, 7th edition.